Optical advantages and function of multifocal spherical fish lenses

Yakir Gagnon,[1,]* Bo Söderberg,[2] and Ronald Kröger[3]

[1]Department of Biology, Duke University, Durham, North Carolina, USA
[2]Department of Theoretical Physics, Lund University, Lund, Sweden
[3]Department of Biology, Lund University, Lund, Sweden
*Corresponding author: 12.yakir@gmail.com

The spherical crystalline lenses in the eyes of many fish species are well-suited models for studies on how natural selection has influenced the evolution of the optical system. Many of these lenses exhibit multiple focal lengths when illuminated with monochromatic light. Similar multifocality is present in a majority of vertebrate eyes, and it is assumed to compensate for the defocusing effect of longitudinal chromatic aberration. In order to identify potential optical advantages of multifocal lenses, we studied their information transfer capacity by computer modeling. We investigated four lens types: the lens of *Astatotilapia burtoni*, an African cichlid fish species, an equivalent monofocal lens, and two artificial multifocal lenses. These lenses were combined with three detector arrays of different spectral properties: the cone photoreceptor system of *A. burtoni* and two artificial arrays. The optical properties compared between the lenses were longitudinal spherical aberration curves, point spread functions, modulation transfer functions, and imaging characteristics. The multifocal lenses had a better balance between spatial and spectral information than the monofocal lenses. Additionally, the lens and detector array had to be matched to each other for optimal function.   © 2012 Optical Society of America

OCIS codes: 330.0330, 330.1070.

1. INTRODUCTION

Vision is an important source of information for many animals, and a variety of different eye types has evolved [1]. Vertebrate eyes are generally similar in design to a photographic camera. However, the optical systems of these eyes are apparently much simpler than a good camera objective that requires a number of lenses to correct for various kinds of optical aberrations. There are at maximum only two lenses in a vertebrate eye: the cornea and the crystalline lens.

In aquatic vertebrates, the cornea is surrounded by water on the outside and the watery aqueous humor on the inside. Both media have similar and relatively high refractive indices and if the cornea is thin, which is the case in most species, its refractive power is negligible [2,3]. The task of focusing light on the retina is thus left to the lens alone. Among the aquatic vertebrates, the lenses of teleosts have received the most attention, mainly because of easy access to fresh material and the simple geometry of the lenses, which are typically spherical [4–6].

Spherical lenses made of homogenous materials (e.g., glass) suffer from longitudinal spherical aberration (LSA). Maxwell was the first to note that fish lenses are almost free of LSA. He suggested that LSA is greatly reduced in fish lenses by a refractive index gradient (RIG), with the highest refractive index (RI) in the center and lowest RI at the surface of the lens [7]. Today we know that such a gradient exists and that it is correlated with the cellular structure of the lens. Vertebrate lenses consist of fiber cells—thin cells that stretch from pole to pole in concentrically arranged layers. Different refractive indices in different layers make up the RIG of the entire lens.

Another optical problem arises from dispersion: the RI of any medium that interacts with light is a function of the wavelength of light passing through it. In consequence, optical systems focusing a wide range of wavelengths (polychromatic light) suffer from longitudinal chromatic aberration (LCA): light of different wavelengths is focused at different distances from the optical system. This leads to chromatic blur on the retina. The blurring effect is most pronounced in optical systems of small f-numbers (i.e., systems with short focal lengths relative to aperture diameter), which have short depth of focus. Fish lenses are powerful, with normalized focal lengths of 2.2–3.3 lens radii [8,9], and the iris does most often not cover any significant part of the lens, such that the f-number is between 1.1 and 1.65.

As a mechanism compensating for the defocusing effect of LCA, many fish lenses have several focal lengths when examined with monochromatic light; i.e., they are multifocal. The lens has concentric shells or zones, each consisting of many cell layers and each with a different focal length. The distances between the focal points along the optical axis are equal to the focal length differences due to LCA between the wavelengths of highest importance to the animals. This means that each of these wavelengths is correctly focused on the retina by a specific zone of the lens. A sharp color image is created on the background of defocused light that has passed through "wrong" zones of the lens [10].

Because of the presence of defocused light, one might think that compensation for the defocusing effect of LCA by the multifocal principle leads to poor image quality and is therefore useful only under specific circumstances. However, the mechanism is present in the eyes of a variety of fishes

[8,10–13] and tetrapods [14–16], which suggests a more general relevance and applicability. We investigated therefore the information transfer capacities of multi- and monofocal lenses.

2. MATERIALS AND METHODS

For the detector array, we used the spatial and spectral characteristics of the trichromatic cone photoreceptor system of *Astatotilapia burtoni* (the African cichlid fish species in which the multifocal principle was discovered; natural), a hypothetical array with narrower spectral sensitivities, but the same wavelengths of maximum absorbance (λ_{max}) and spatial resolution (camera), and another hypothetical array with narrow sensitivities that were offset from the *A. burtoni* λ_{max} values (mismatch) (Fig. 1). We used computer modeling to compare the optical properties of four lens types, representing the lens of *A. burtoni* (burtoni lens), a monofocal lens exactly focusing light of intermediate wavelength (monofocal lens), a hypothetical lens with sharply defined zones of different focal lengths (step-function lens), and another hypothetical lens in which the wavelengths focused by the sharply defined zones were slightly offset from the λ_{max} values of the photoreceptors (mismatch lens). For each lens, we started with the monochromatic LSA, calculated the RIG of a spherical model lens with such an LSA, and used the lens model to determine the polychromatic point spread function (PSF), modulation transfer function (MTF), and imaging of a hyperspectral image stack. Comparing between the natural and monofocal lenses allows us to quantify the disadvantages/advantages a multifocal lens has over a monofocal one. The step-function lens tests the multifocal principle in its simplest interpretation (three distinct layers each responsible for focusing one color-channel). The mismatch retina and lens answer the question of how precisely the lens and retina need to match each other for the multifocal principle to work properly.

A. Model Lenses

The basic properties of the model lenses were chosen according to results on the morphology and optical properties of fish lenses [17,18]. The RI of the surrounding medium was set to 1.334 (equal to that of the aqueous and vitreous humours). The thickness of the lens capsule was 0.009 lens radius (R), its RI was 1.394. A zone of constant index (1.362) extended from the capsule inwards to 0.94 R, such that the RIG ranged from 0.94 R to the lens center [17]. The RIs mentioned above were valid for 633 nm. LCA was accounted for by using the dispersion function by Gagnon *et al.* [19] that is suitable for vertebrate ocular media in general and *A. burtoni* lenses in
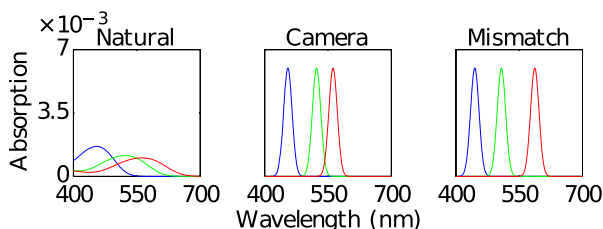

Fig. 1. (Color online) Absorption curves of the three retinas: natural, camera, and mismatch. The *x*-axis denotes the wavelength in nanometers. The *y*-axis is the absorption. From right to left, the red, green, and blue photoreceptors are color-coded. Note that the curves are normalized so that their sum equals 1.
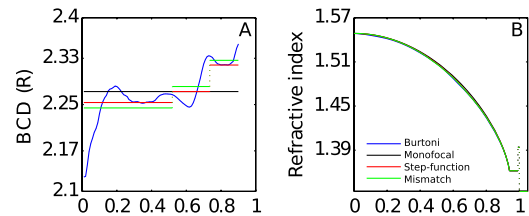

Fig. 2. (Color online) A, LSA curves of the four lenses. The different lenses are color-coded (legend in panel B): Burtoni (blue), monofocal (black), step-function (red), mismatch (green). The *x*-axis denotes the BEP, while the *y*-axis is the BCD of the laser beam; both are in lens radius (R) units (i.e., 1 represents the lens' surface). B, RIG of the four lenses. The lenses are color-coded as in A. The *x*-axis is the distance from the lens center in units of R. The *y*-axis is the RI at wavelength 633 nm.

particular. The spherically curved retina was concentric to the lens and positioned at 2.233 R from the lens center [18].

We created four different model lenses, named the Burtoni lens, the monofocal lens, the step-function lens, and the mismatch lens (Fig. 2). The lenses' optical properties were defined by their LSA curves. A measured LSA curve describes the deflection of a laser beam as a function of where the beam entered the lens. The independent variable of this function is the lateral distance between the optical axis of the lens and the entering beam (beam entrance position, BEP). The dependent variable is the distance between the center of the lens and the point where the exiting beam—deflected by the lens—intercepted the optical axis (back center distance, BCD). Because of the inverse relationship of wavelength and RI, and thus refractive power, lens zones with longer BCDs focus shorter wavelengths and vice versa. The RIG of a spherical lens can be inferred from its LSA curve using the inverse Abel transform [17,18,20–29]. The reader is advised to consult the mentioned reports [17,21,28] for detailed descriptions of the mathematical procedures. All calculations were performed in Matlab (2010a) using the chebfun package [30], which allows for high accuracy and analytical-like solutions.

The Burtoni lens was a model of a natural multifocal lens [10] and had an LSA curve as measured in *A. burtoni* lenses [18]. The monofocal lens focused the wavelength of maximum absorbance (λ_{max}) of *A. burtoni* middle wavelength sensitive cones (523 nm [31]). The step-function lens had three zones, each focusing one of the three λ_{max} of the cones of *A. burtoni*. The inner zone focused 455 nm, the middle zone 523 nm, and the outer zone 562 nm [31]. The mismatch lens focused slightly different wavelengths, but with an equal mean λ_{max}. The wavelengths in exact focus were 445 nm for the inner zone, 508 nm for the middle zone, and 587 nm for the outer zone. The area of each zone devoted to focusing a certain wavelength controls the amount of focused light at that wavelength, where larger zones result in more light and vice versa. More focused light leads to sharper images at that wavelength. The zone areas accepting light were therefore set equal; i.e., zone width decreased with increasing zone radius (a square root function).

B. Ray-Tracing and Sampling

Ray-tracings were performed for polychromatic light (50 wavelengths between 400 and 700 nm) using each lens's RIG at 633 nm, the dispersion function by Gagnon *et al.*

[19], and the Abel transform. In order to account for the larger contributions of more peripheral rays to retinal illumination in a real three-dimensional imaging situation, the ray entrance positions in the two-dimensional model were distributed according to a square root transformation. PSFs calculated from 10^6 rays (i.e., 10^6 BEP values) were sufficiently stable when compared to analytical approximations of the PSFs. The deflection angle of a refracted ray was used to determine the angular deviation between the optical axis and the point where the incoming ray intercepted the retina.

With a focal length of 2.233 R, a lens radius of 1.5 mm, and an estimated photoreceptor cell density of 52 500 cells per mm^2 [31], the inter-receptor angle, $\Delta\theta$, in the *A. burtoni* retina was approximately 0.037°. This value was used as the bin width for ray sampling in the retinal plane, with the central bin centered on the optical axis (0°). Since increasing deviation angles correspond to a larger number of photoreceptors/pixels sharing the incoming light, each ray's contribution to a bin's illumination was weighted accordingly. The weighting factor was $\frac{1}{4\pi \sin^2 \frac{\Delta\theta}{4}}$ for the central bin and $\frac{1}{4\pi \sin\theta \sin \frac{\Delta\theta}{2}}$ for all other bins, where $\Delta\theta$ was the inter-receptor angle and θ was the angle between the optical axis and each consecutive receptor. This procedure resulted in a discrete PSF at each wavelength describing how light from a point in object space illuminates the photoreceptors after being focused by the lens. Since light intensity was equal among wavelengths (white light) and to maintain the brightness of the convolved image, the PSFs were divided by their sum, namely 10^6. The illumination of the central pixel (i.e., $-\frac{\Delta\theta}{2} \leq \theta \leq \frac{\Delta\theta}{2}$), $I(\theta_0, \lambda)$, was used as a focus indicator. $I(\theta_0, \lambda)$ is high if the image of a point object is well-focused. The distribution of the central pixel intensities as a function of wavelength describes the effects of LCA on image quality.

The MTF of a lens was determined by (the magnitude of) fast Fourier transformation of the PSF. MTFs were calculated for spatial frequencies from 0 to 27 cycles per degree, which was the highest possible frequency (cutoff frequency) set by the sampling interval of 0.037°. An MTF describes how quickly image contrast deteriorates with increasing spatial frequency.

C. Hyperspectral Image
A hyperspectral image is a stack of image tiers, where each tier shows the same scene in a different wavelength interval. Typically, the wavelength intervals are narrow (10 nm), allowing for high spectral resolution with stacks containing up to 30 tiers or even more [32]. We created an artificial hyperspectral image to illustrate the performances of the different model lenses. In a checkerboard pattern (201×201 squares), each square patch was assigned a relative reflectance spectrum in a pseudorandom manner such that no adjacent (vertically, horizontally, and diagonally) squares had the same spectrum. The spectra were taken from more than 200 species of Hawaiian, Australian, and Caribbean reef fish [33]. The colored checkerboard pattern was spatially transformed by squaring the polar radial component of the location of each vertex. This spatial transformation increased the scope of spatial frequencies the hyperspectral image included; by stretching the squares in the image center and packing the peripheral squares closer together, we achieved low, mid, and high spatial frequencies all in the same image. The resulting mesh was not square and therefore cropped to fit an image of 600×600

pixels. Only the central 500×500 pixels were used in the final RGB images to avoid zero-padding artifacts around the edges of the image (a dark frame surrounding the image). Since each image pixel represented one photoreceptor, this hyperspectral image occupied 18.5° on the retina, resulting in spatial frequencies ranging from approximately 1 to 10 cycles per degree (note that the model retina had a sampling density of 27 photoreceptors per degree). The final hyperspectral image was 500×500 pixels large with 50 wavelengths from 400 to 700 nm.

D. Spatial and Spectral Filtering
Imaging of a scene by a lens leads to spatial filtering and the amount of detail loss depends on the quality (PSF) of the lens. We convolved each wavelength tier of the hyperspectral image with the PSF of the model lens at the same wavelength (convolution of two images results in a new image where each of its pixels is the sum of the product of the region around that pixel's location in the first image with the second image). The next step was spectral filtering according to the sensitivities of the photoreceptors/pixels in the retina. We used three different retinas. These were named the natural retina, the camera retina, and the mismatch retina.

In the natural retina, there were three spectral photoreceptor/pixel types with the λ_{max} of the cones of *A. burtoni* (455, 523, and 562 nm; [31]). Absorption spectra were estimated using the Govardovskii templates for visual pigments ([34], Fig. 1) with published histological data and photonic properties of the cones [31,35]. All absorption curves were divided by their sum in order to avoid unequal brightness between the image channels (requiring white-balancing). Corrections for adaptive processes and retinal processing were not applied. The pixels in the camera retina had the same λ_{max} values as the natural retina, but with bell-shaped (Gaussian) absorption spectra. The Gaussian functions had standard variation of about 14 nm, resulting in relatively little overlap between spectral channels (Fig. 1). The mismatch retina had the same bell-shaped absorption spectra, but with different λ_{max} values than that of the other two retinas, namely 445, 508, and 587 nm (Fig. 1).

After multiplying each pixel in each tier with the pixel's absorption spectrum, the stimulations of corresponding pixels were summed across the entire stack. This was done separately for each of the three spectral pixel types, resulting in an RGB image. The same procedure of spectral filtering and stimulation summing was also applied on the original hyperspectral image (i.e., the hyperspectral image prior to modulation by the lens). These images represented the best possible scenarios with regard to lens quality and were used as references for comparisons. All final images were multiplied by 255 and converted to UINT8 images (since the maximum spectral reflectance modeled in the hyperspectral image was never larger than 1, pixel intensities were less than 1 as well).

E. Comparing the Filtered Images
In each image, pixels of the same stimulation level (0–255) were counted separately for each channel. A broad and flat distribution of pixel counts indicated a sharp and patchy image, i.e., a good representation of the original unfiltered image. If spatial and spectral filtering evened out the differences
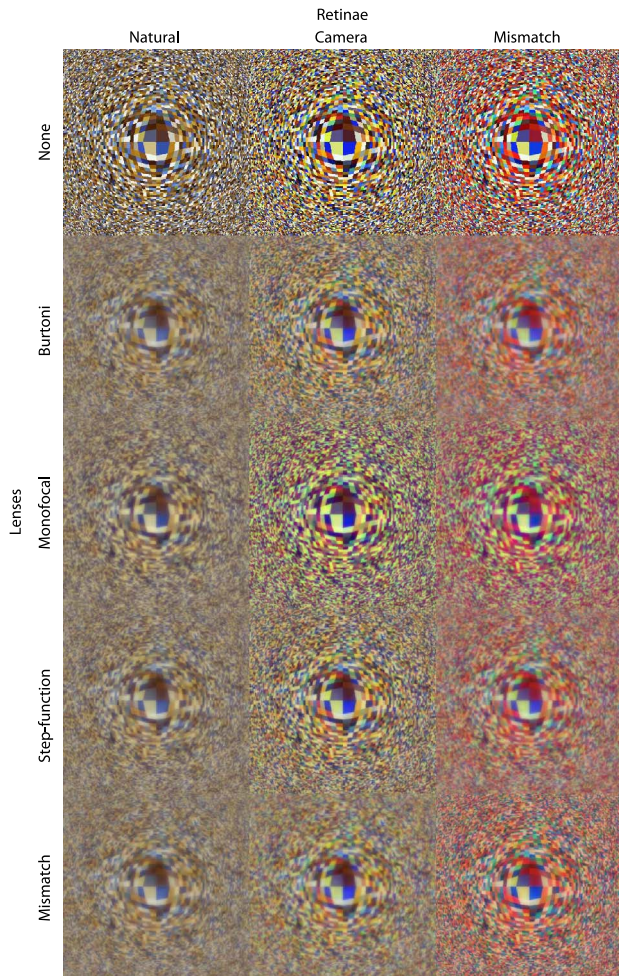
Fig. 3. (Color online) A hyperspectral image stack was imaged by the four lenses and sampled by the three detector arrays. The lenses are displayed per row (from top to bottom: none, Burtoni, monofocal, step-function, and mismatch), and the arrays are per column (from left to right: natural, camera, and mismatch). The first row, "none," includes the hyperspectral images sampled by the arrays without any optical filtering (i.e., these retained all spatial information before being sampled). Note the greenish hue of the monofocal row. The mismatch row is sharper when sampled with the mismatch retina, while it produces a blurrier image with the other two retinae. The opposite is true for the step-function lens. This figure displays the estimated signals received at the first layer of the retina. Post processing (e.g., white-balancing, histogram equalization, opponent processing, etc.) that occurs in subsequent layers (both morphological and physiological) may considerably change the information transmitted to the brain. It is therefore important to remember that certain image aspects being presented here in their "raw" form, such as haziness, can be corrected for higher up in the visual pathway. Because of the raw nature of this representation, certain aspects of these images can be misleading. The false contrast perceived in the monofocal lens sampled by the camera array does not represent a real increase in the information content of that image (see Fig. 4 for a better understanding of the comparison between the images).

between the pixels in the original image, the distribution of pixel counts was narrow and pointed [36]. This method is reliable when comparing intrinsically similar images with sharp borders between differently colored areas. Corresponding slices from the camera retina images were juxtaposed to a close-up wheel pattern to facilitate comparisons by visual inspection (Figs. 3 and 4).
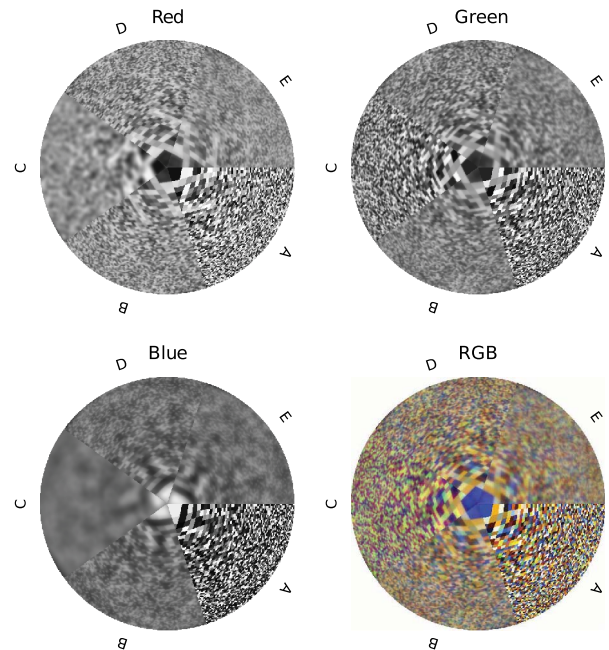

Fig. 4. (Color online) A comparison of corresponding slices (enlarged) taken from each row in the camera array column in Fig. 3 (second column). The slices were rotated and fitted into a wheel to facilitate comparisons. The slices are from the none, Burtoni, monofocal, step-function, and mismatch images in Fig. 3 and are labeled A, B, C, D, and E, respectively. The red, green, and blue wheels display the three color channels present in the RGB wheel. Note the poor color representation in the monofocal slice, where all the smaller patches have shades of green or purple. The mismatch slices have reduced contrast in all three channels. No obvious differences are present between the Burtoni and step-function slices.

3. RESULTS

A. PSF and MTF

The Burtoni model lens created complex patterns of retinal illumination with peaks in the PSFs, i.e., high values for $I(\theta_0, \lambda)$ (light intensity on the retina in the optical axis as a function of wavelength), at or close to the λ_{max} of the cones of *A. burtoni* (Fig. 5). This mirror's results are obtained by using measured LSAs [10], indicating that the Burtoni lens model recreated the optical properties of real *A. burtoni* lenses throughout the spectrum. The monofocal lens created a sharp peak at 523 nm and the PSFs broadened rapidly towards shorter and longer wavelengths. The PSFs of the step-function lens had three distinct peaks at the λ_{max} values the lens was optimized for (455, 523, and 562 nm). The peak in the blue range, created by the outmost zone in the lens, was considerably sharper than the peaks at longer wavelengths (Fig. 5). The $I(\theta_0, \lambda)$ of the mismatch lens peaked at 445, 508, and 587 nm. The peak in the long wavelength range was broader than the equivalent peak in the step-function lens, indicating a wider range of wavelengths being in sharp focus.

The MTFs showed high contrast (e.g., the step-function lens created about 0.96 contrast at 562 nm) for spatial frequencies as high as 27 cycles per degree, i.e., the maximum sampling frequency. This was true, however, only at the wavelengths where the PSFs had high $I(\theta_0, \lambda)$ values (Fig. 5). The Burtoni lens had lower contrast (about 0.78 at 562 nm) for those wavelengths at the spatial cutoff frequency, but higher contrast for wider ranges of wavelengths (Fig. 5).
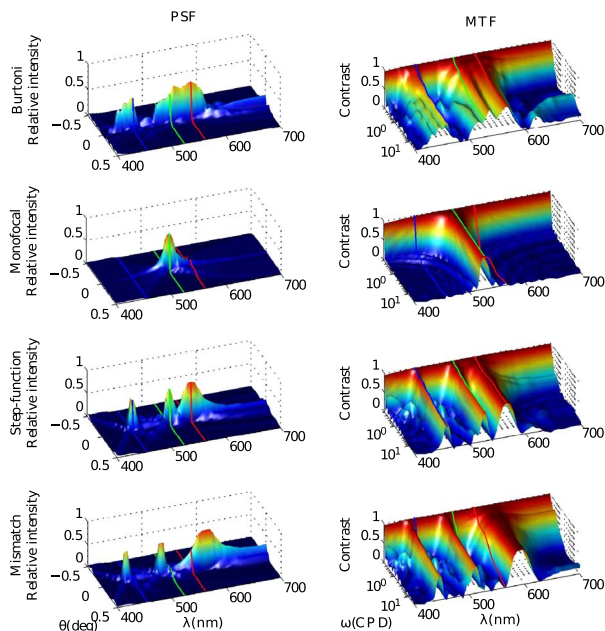
Fig. 5. (Color online) Left column shows the PSFs of all four lenses and the MTF are on the right. Each row depicts one lens; from top to bottom: Burtoni, monofocal, step-function, and mismatch. The x-axis in the PSF panels is the wavelength of light. The y-axis is the spread angle in degrees, i.e., the angle between the intersection of the optical axis with the retina, the nodal point of the lens, and the intersection of the exiting ray of light with the retina. This angle is a measure for the deviation from a perfect focus. The z-axis is the relative light intensity on the retina surface (before it gets absorbed by the photoreceptor). The x-axis in the MTF panels is the wavelength of light. The y-axis is the spatial frequency in units of cycles per degree (logarithmic scale) of the signal being focused. This frequency has a cutoff at 27 cycles per degree, matching the maximum sampling frequency by cone photoreceptors in the *A. burtoni* retina. The z-axis represents the contrast at each wavelength. The surface color denotes the height along the z-axis in all panels. The three $\lambda_{\max}$ values of *A. burtoni* cones are represented as color-coded lines superimposed on the surfaces.

B. Images

Filtering a hyperspectral image stack (50 images between 400 and 700 nm) by the PSFs of the lenses and the absorption functions of the detector arrays resulted in an RGB image for each lens/array combination (Fig. 3). All lens/array combinations created equally bright images because the sums of the PSFs and absorption curves were all equal to 1. The camera and mismatch arrays produced more saturated colors than the natural array. The patches in the images detected by the mismatch array were red tinted, while the monofocal lens produced green tinted images, indicating an imbalance between the spectral channels. The image created by the step-function lens was more detailed with the camera array than it was with the mismatch array. The opposite was true for the mismatch lens. Because of the broad spectral sensitivities of fish cone photoreceptors, there was least variation between the different images sampled by the natural array.

A close-up of the three color channels of the images sampled by the camera array (Fig. 4) shows that while the monofocal lens' image was well-focused for the green channel, it was severely defocused for the red and especially the blue channel. Images created by the mismatch lens were defocused for all three channels. All lenses created most defocus in the blue channel.

The image histograms (Fig. 6) show that the Burtoni lens created the highest contrast in combination with the camera array. The monofocal lens had a broad pixel intensity distribution in the green channel, indicating high contrast with the camera array and slightly lower contrast with the mismatch array. If sampled by the natural array with broad spectral sensitivities, this channel was relatively defocused. The red and blue channels, however, had low contrast with narrow and pointy histograms, most pronounced for the mismatch array. As expected from the images in Fig. 3, the image created by the step-function lens had narrower histograms with the mismatch array, while the opposite was true for the mismatch lens. The red channel histograms of the mismatch array were all shifted to the right, indicating higher pixel intensities than found in the red channels of both other arrays.

4. DISCUSSION

A. Model Performance

The performances of the multifocal fish lens models we present here are conservative estimates. The LSA curve used for the Burtoni lens model is an average of 21 lenses [10]. Furthermore, the diameter of the laser beam used in the original measurements (100 μm [18]) limited the spatial resolution of the results. Individual LSAs may have finer detail and such details may be of relevance for optimum lens performance. However, individual LSA curves also reflect measurement errors, such that we consider the average curve to be more reliable for the purpose of gaining a general understanding of the function of multifocal biological lenses.

The distinct refractive zones of the step-function lens brought the $\lambda_{\max}$ of the detector array pixels into exact focus. There was no evident improvement of spatial and spectral information transfer compared to the Burtoni lens (Figs. 4 and 6) based on averaged data. A natural fish lens with a smooth LSA curve may transfer more information than the step-function lens with well-defined refractive zones with sharp transitions between focal lengths. In fish there is a large variety of multifocal lenses, including ones with several refractive zones focusing similar spectral ranges [10,11,37–40]. Analysis of these phenomena and adaptations was beyond the scope of our work.

B. Dispersion and Depth of Focus

The shapes of the PSFs resulted mainly from two factors and their interaction: chromatic dispersion and depth of focus. Dispersion is a nonlinear phenomenon, being stronger for shorter wavelengths than for longer ones. The monofocal lens therefore creates more defocus at short wavelengths than at long wavelengths. The nonlinearity of dispersion also explains why the blue channel in the RGB images was always the most defocused one. This kind of wavelength dependent defocusing occurred in all lenses (Fig. 5).

The order of lens zones focusing specific wavelengths influences the performance of the lens. Depth of focus is inversely correlated to the distance between the incoming beam of light and the optical axis of the system, i.e., BEP. Smaller BEP values correlate with longer depth of focus and fewer aberrations. Thus, discrepancies between the wavelength of the incoming light and the intended wavelength are less detrimental for smaller BEPs than for larger BEPs. Both the step-function and mismatch lenses had shorter BCDs for smaller
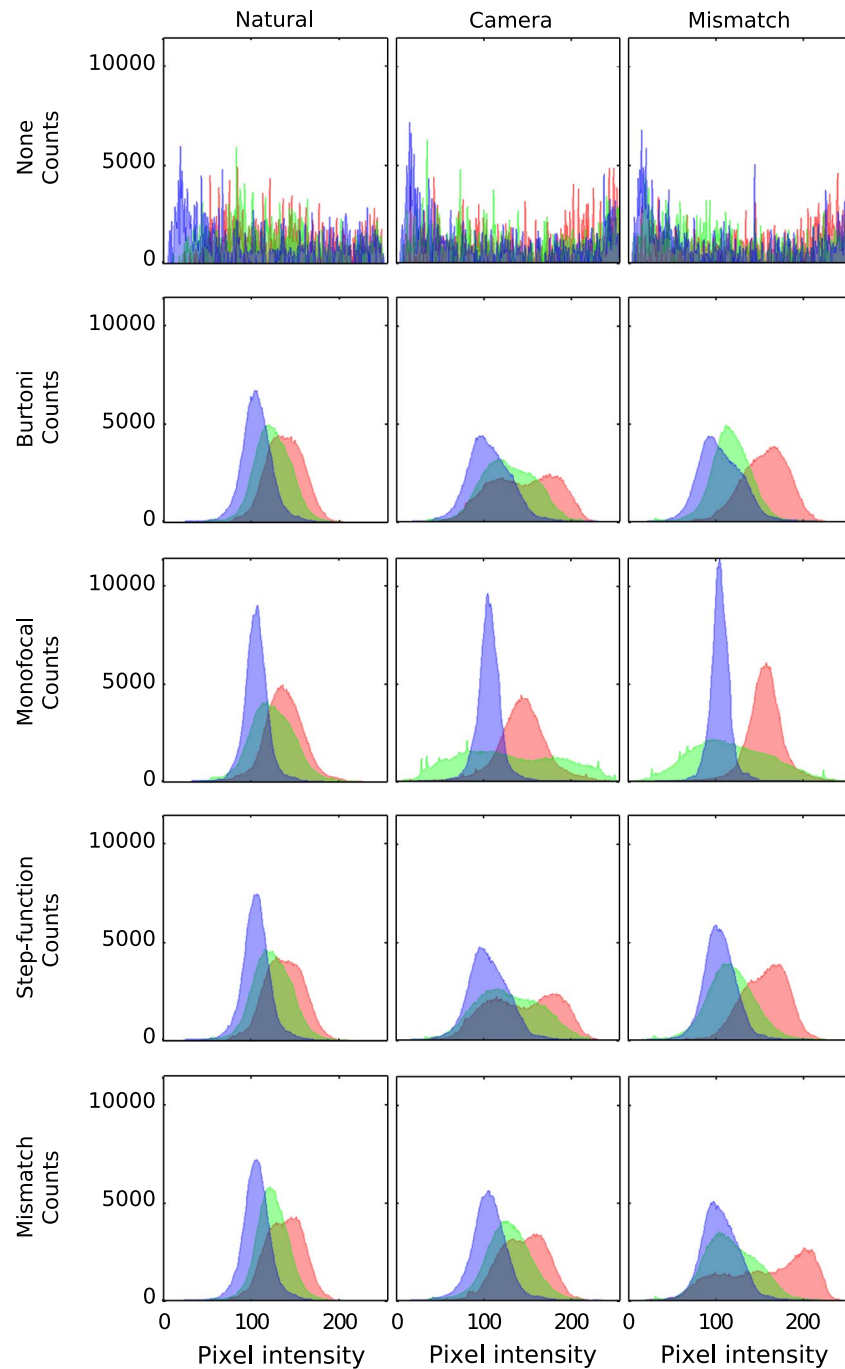
Fig. 6.   (Color online) Image histograms for the filtered and sampled hyperspectral images presented in Fig. 3. The lenses are displayed per row (from top to bottom: none, Burtoni, monofocal, step-function, and mismatch), and the arrays are per column (from left to right: natural, camera, and mismatch). The first row includes the histogram of the hyperspectral images sampled by the arrays without any optical filtering (i.e., these retained all spatial information before being sampled). The x-axis is the pixel intensity ranging from 0 to 255 (2^8 intensity steps). The y-axis is the frequency of pixels with the corresponding intensity. The trichromatic arrays have one histogram for each of their color channels, red, green, and blue (color-coded). The histograms describe the distribution of pixel intensities in the images. This can be used to compare contrast between similar images. A broad distribution of pixel intensities, such as in the histogram of the unfiltered images (none), results in a higher contrast. A pointy narrow histogram indicates that the image has a very limited range of pixel intensities resulting in a bland image poor in contrast. Notice that while the green channel of the monofocal image sampled by the camera array has a broad histogram indicating high contrast, its red and blue channels are pointy and narrow, indicating low contrast.

BEPs; i.e., they were focusing longer wavelengths closer to the optical axis (Fig. 2). Because of this and in addition to the effects of dispersion, focus deteriorated faster for short wavelengths than for long wavelengths, explaining the wider ranges of focused long wavelengths and the narrower short wavelength bands (Fig. 5).

The amount of light being focused at a certain wavelength is determined by the area of the lens zone devoted to focusing that specific wavelength and affects the contrast of an image at that wavelength. Since each lens zone can be used for only one wavelength, the size of a zone assigned to focus a specific wavelength limits the amount of light focused at other

wavelengths. With depth of focus, dispersion, and photo-receptor size all affecting the PSF and contrast, the optimal allocation of lens zones is not trivial. It is clear, however, that dividing the lens into three zones of equal aperture areas and each focusing a specific wavelength (e.g., the step-function lens) improves the functionality of the lens in comparison to a monofocal lens. Three about equally focused channels transfer more information than one well-focused channel combined with two heavily defocused channels (Figs. 4 and 6).

C. Peripheral Visual Filtering

Lens and retina can both transfer only limited amounts of information from the environment to the nervous system of a fish. In addition, the type and amount of information transferred is dependent on the functional tuning between the lens and retina. Our results illustrate this in striking ways. Contrast dropped quickly with increasing spectral distance from the $\lambda_{\max}$ of the green channel in the monofocal lens case. This caused the well-localized high pixel intensities in the green channel to stand out against the heavily defocused images in the other two channels, resulting in green-and-purple contrasts in images created by the monofocal lens (slice C in Fig. 4). The multifocal lenses, on the other hand, created relatively high contrasts at several wavelength intervals (Figs. 6 and 2). Multifocal lenses thus improve the transfer of spectral information at the cost of some loss of spatial information. In animals with color vision and eyes of small f-numbers, i.e., short depth of focus, this tradeoff between spatial and spectral information seems to be more favorable with multifocal lenses. Many vertebrate species, both aquatic and terrestrial, have such lenses [10,11,14–16,37–41].

High spatial frequencies in the retinal image can lead to aliasing problems. For wavelengths where $I(\theta_0, \lambda)$ was high, the MTFs indicated high contrasts at the retina's cutoff frequency. Image contrast deteriorated significantly only for spatial frequencies considerably higher than the cutoff frequency of the retina. Special pixel patterns reduce the aliasing problem, but cannot eliminate it [42]. Overlap in spectral sensitivities and crosstalk between spectral channels can also reduce aliasing [42] but lead to problems with image quality. Images sampled by the natural retina were relatively similar (least variation in the quality of the images created by different lenses, Figs. 4 and 2) and the Burtoni lens's MTFs seemed to be most closely matched to the retina's limited spatial resolution.

Overlap in spectral sensitivities in the natural retina produced blurrier images than sampling by the camera and mismatch retinas (Fig. 4). However, less overlap between the spectral sensitivities can also lead to artifacts, most prominently poor color reproduction. The red hues in the images of the mismatch retina were caused by the larger separation of the red sensitive photoreceptors from the green ones, causing red colors to be more saturated (column mismatch in Fig. 4).

Wehner introduced the notion of "peripheralization"; unnecessary information should be filtered out as early as possible in the sensory pathway [43]. The Burtoni lens can be regarded as an example for this: it neither focuses wavelengths not being absorbed by the retina, nor does it focus spatial frequencies much higher than the cutoff frequency of the retina.

D. Adaptation and Regulation

There is a wide variation of visual pigments and visual pigment combinations in fish retinae [44,45]. The evolutionary adaptation of visual pigments occurs by genetic changes, either in the expression of pigment genes [46] or mutations in the opsin genes leading to amino acid substitutions in the opsin molecule [47–51]. Here we have shown that the optical properties of the lens should match the spectral composition of the retina in order to maximize optical performance, indicating that there should be an equally large variation in the optical properties of fish lenses, and this has indeed been observed [10,11,37–40]. Interestingly, changes in the optical properties of fish lenses can be induced by environmental parameters and take place within a few hours to months [13,52]. This implies that the matching of lens optical properties to the requirements of the retina may be an active process, involving signaling from the retina to the lens. One such signaling pathway involving dopamine has a role in the optical changes occurring in the lenses of the South American cichlid fish *Aequidens pulcher* between day and night [13,53,54].

It is interesting to note that lenses differing in LSA, PSF, MTF, and imaging properties have relatively small differences in their RIGs (Fig. 5E). These minute differences are caused by small differences in crystalline protein concentrations in corresponding parts of the lens. This indicates that well-tuned regulatory mechanisms are required in order to maintain and adjust the RIG and thus the functionality of the lens. This is particularly impressive and perplexing because of the denucleation of lens fiber cells during maturation.

REFERENCES

1. M. F. Land and D. E. Nilsson, *Animal Eyes*, Animal Biology Series (Oxford, 2002).
2. T. Mandelman and J. G. Sivak, "Longitudinal chromatic aberration of the vertebrate eye," Vis. Res. **23**, 1555–1559 (1983).
3. L. Matthiessen, "Beiträge zur dioptrik der kristalllinse," X. Zeitschrift für vergleichende Augenheilkunde **7**, 102–146 (1893).
4. R. J. Pumphrey, *Concerning Vision* (Cambridge University, 1961), pp. 193–208.
5. J. G. Sivak and C. A. Luer, "Optical development of the ocular lens of an elasmobranch *Raja eglanteria*," Vis. Res. **31**, 373–382 (1991).
6. G. L. Walls, *The Vertebrate Eye and its Adaptive Radiation* (Cranbrook, 1964).
7. J. Maxwell, "Some solutions of problems 2," Cambridge Dublin Math. J. **8**, 188–195 (1854).
8. R. H. H. Kröger, K. A. Fritsches, and E. J. Warrant, "Lens optical properties in the eyes of large marine predatory teleosts," J. Comp. Physiol. A **195**, 175–182 (2009).
9. L. Matthiessen, "Ueber die beziehungen, welche zwischen dem brechungsindex des kerncentrums der krystalllinse und den dimensionen des auges bestehen," Pflüger's Archiv. **27**, 510–523 (1882).
10. R. H. H. Kröger, M. C. W. Campbell, R. D. Fernald, and H. J. Wagner, "Multifocal lenses compensate for chromatic defocus in vertebrate eyes," J. Comp. Physiol. A **184**, 361–369 (1999).
11. B. Karpestam, J. Gustafsson, N. Shashar, G. Katzir, and R. H. H. Kröger, "Multifocal lenses in coral reef fishes," J. Exp. Biol. **210**, 2923–2931 (2007).
12. P. E. Malkki, E. Löfblad, and R. H. H. Kröger, "Species-specific differences in the optical properties of crystalline lenses of fishes," in *ARVO Annual Meeting Abstract Search and Program Planner 2003* (2003), p. 3483.
13. J. M. Schartau, B. Sjögreen, Y. L. Gagnon, and R. H. H. Kröger, "Optical plasticity in the crystalline lenses of the cichlid fish *Aequidens pulcher*," Curr. Biol. **19**, 122–126 (2009).

14. F. D. Hanke, R. H. H. Kröger, U. Siebert, and G. Dehnhardt, "Multifocal lenses in a monochromat: the harbour seal," J. Exp. Biol. **211**, 3315–3322 (2008).
15. O. E. Lind, A. Kelber, and R. H. H. Kröger, "Multifocal optical systems and pupil dynamics in birds," J. Exp. Biol. **211**, 2752–2758 (2008).
16. T. Malmström and R. H. H. Kröger, "Pupil shapes and lens optics in the eyes of terrestrial vertebrates," J. Exp. Biol. **209**, 18–25 (2006).
17. Y. L. Gagnon, B. Söderberg, and R. H. H. Kröger, "Effects of the peripheral layers on the optical properties of spherical fish lenses," J. Opt. Soc. Am. A **25**, 2468–2475 (2008).
18. R. H. H. Kröger, M. C. W. Campbell, R. Munger, and R. D. Fernald, "Refractive index distribution and spherical aberration in the crystalline lens of the African cichlid fish *Haplochromis burtoni*," Vis. Res. **34**, 1815–1822 (1994).
19. Y. L. Gagnon, R. H. H. Kröger, and B. Söderberg, "Adjusting a light dispersion model to fit measurements from vertebrate ocular media as well as ray-tracing in fish lenses," Vis. Res. **50**, 850–853 (2010).
20. R. H. H. Kröger and M. C. W. Campbell, "Dispersion and longitudinal chromatic aberration of the crystalline lens of the African cichlid fish Haplochromis burtoni," J. Opt. Soc. Am. A **13**, 2341–2347 (1996).
21. M. C. W. Campbell, "Measurement of refractive index in an intact crystalline lens," Vis. Res. **24**, 409–415 (1984).
22. M. C. W. Campbell and P. J. Sands, "Optical quality during crystalline lens growth," Nature **312**, 291–292 (1984).
23. B. K. Pierscionek, "Nondestructive method of constructing 3-dimensional gradient index models for crystalline lenses 1. theory and experiment," Am. J. Optom. Phys. Opt. **65**, 481–491 (1988).
24. B. K. Pierscionek, "Refractive index of the human lens surface measured with an optic fibre sensor," Ophthalmic Res. **26**, 32–35 (1994).
25. B. K. Pierscionek, "The refractive index along the optic axis of the bovine lens," Eye **9**, 776–782 (1995).
26. B. K. Pierscionek and R. C. Augusteyn, "The refractive index and protein distribution in the blue eye trevally lens," J. Am. Optometric Assoc. **66**, 739–43 (1995).
27. A. Fletcher, T. Murphy, and A. Young, "Solutions of two optical problems," Proc. R. Soc. A **223**, 216–225 (1954).
28. P. L. Chu, "Nondestructive measurement of index profile of an optical-fibre preform," Electron. Lett. **13**, 736–738 (1977).
29. K. F. Barrell and C. Pask, "Nondestructive index profile measurement of noncircular optical fibre preforms," Opt. Commun. **27**, 230–234 (1978).
30. L. N. Trefethen, N. Hale, R. B. Platte, T. A. Driscoll, and R. Pachón, Chebfun version 3. Oxford University. http://www.maths.ox.ac.uk/chebfun/ (2009).
31. R. D. Fernald and P. A. Liebman, "Visual receptor pigments in the African cichlid fish *Haplochromis burtoni*," Vis. Res. **20**, 857–864 (1980).
32. J. K. Lein, "Hyperspectral sensing," in *Environmental Sensing: Analytical Techniques for Earth Observation* (Springer, 2012), p. 213.
33. N. J. Marshall, K. Jennings, W. N. McFarland, E. R. Loew, G. S. Losey, and W. L. Montgomery, "Visual biology of Hawaiian coral reef fishes. II. Colors of Hawaiian coral reef fish," Am. Soc. Ichthyol. Herpetol. **3**, 455–466 (2003).
34. V. I. Govardovskii, N. Fyhrquist, T. O. M. Reuter, D. G. Kuzmin, and K. Donner, "In search of the visual pigment template," Vis. Neurosci. **17**, 509–528 (2000).
35. E. Warrant and D. Nilsson, "Absorption of white light in photoreceptors," Vis. Res. **38**, 195–207 (1998).
36. J. Stark and W. Fitzgerald, "An alternative algorithm for adaptive histogram equalization," Graph. Models Image Process. **58**, 180–185 (1996).
37. P. E. Malkki and R. H. H. Kröger, "Visualization of chromatic correction of fish lenses by multiple focal lengths," J. Opt. A **7**, 691–700 (2005).
38. O. S. E. Gustafsson, S. P. Collin, and R. H. H. Kröger, "Early evolution of multifocal optics for well-focused colour vision in vertebrates," J. Exp. Biol. **211**, 1559–1564 (2008).
39. O. S. Gustafsson, P. Ekström, and R. H. Kröger, "A fibrous membrane suspends the multifocal lens in the eyes of lampreys and African lungfishes," J. Morphol. **271**, 980–989 (2010).
40. R. H. H. Kröger, "Physiological optics in fishes," in *Encyclopedia of Fish Physiology: From Genome to Environment* (Elsevier, 2011) pp. 102–109.
41. L. S. V. Roth, L. Lundström, A. Kelber, R. H. H. Kröger, and P. Unsbo, "The pupils and optical systems of gecko eyes," J. Vision **9**(3): 27, 1–11 (2009).
42. R. H. H. Kröger, "Anti-aliasing features in fish retina," Investig. Ophthalmol. Vis. Sci. **45**, 2785 (2004).
43. R. Wehner, "'matched filters'—neural models of the external world," J. Comp. Physiol. A**161**, 511–531 (1987).
44. J. N. Lythgoe, W. R. A. Muntz, J. C. Partridge, J. Shand, and D. M. B. Williams, "The ecology of the visual pigments of snappers (Lutjanidae) on the great barrier reef," J. Comp. Physiol. A **174**, 461–467 (1994).
45. J. Bowmaker, V. Govardovskii, S. Shukolyukov, J. L. Zueva, D. Hunt, V. G. Sideleva, and O. G. Smirnova, "Visual pigments and the photic environment: the cottoid fish of Lake Baikal," Vis. Res. **34**, 591–605 (1994).
46. J. W. Parry, K. L. Carleton, T. Spady, A. Carboo, D. M. Hunt, and J. K. Bowmaker, "Mix and match color vision: tuning spectral sensitivity by differential opsin gene expression in Lake Malawi cichlids," Curr. Biol. **15**, 1734–1739 (2005).
47. J. K. Bowmaker and D. M. Hunt, "Evolution of vertebrate visual pigments," Curr. Biol. **16**, R484–R489 (2006).
48. Y. Shichida and T. Matsuyama, "Evolution of opsins and phototransduction," Phil. Trans. R. Soc. B **364**, 2881–2895 (2009).
49. A. E. Trezise and S. P. Collin, "Opsins: evolution in waiting," Curr. Biol. **15** R794–R796 (2005).
50. S. Yokoyama, "Molecular evolution of vertebrate visual pigments," Prog. Retinal Eye Res. **19**, 385–419 (2000).
51. K. E. O'Quin, C. M. Hofmann, H. A. Hofmann, and K. L. Carleton, "Parallel evolution of opsin gene expression in African cichlid fishes," Mol. Biol. Evol. **27**, 2839–2854 (2010).
52. R. H. H. Kröger, M. C. W. Campbell, and R. D. Fernald, "The development of the crystalline lens is sensitive to visual input in the African cichlid fish, Haplochromis burtoni," Vis. Res. **41**, 549–559 (2001).
53. J. M. Schartau, R. H. H. Kröger, and B. Sjögreen, "Short-term culturing of teleost crystalline lenses combined with high-resultotion optical measurements," Cytotechnology **62**, 167–174 (2010).
54. J. M. Schartau, R. H. H. Kröger, and B. Sjögreen, "Dopamine induces optical changes in the cichlid fish lens," PLoS ONE **5**, e10402 (2010).